



A deep neural network for classification of melt-pool images in metal additive manufacturing

Ohyung Kwon¹ · Hyung Giun Kim¹ · Min Ji Ham¹ · Wonrae Kim¹ · Gun-Hee Kim¹ · Jae-Hyung Cho² · Nam Il Kim² · Kangil Kim³

Received: 12 April 2018 / Accepted: 10 October 2018 / Published online: 17 October 2018
© Springer Science+Business Media, LLC, part of Springer Nature 2018

Abstract

By applying a deep neural network to selective laser melting, we studied a classification model of melt-pool images with respect to 6 laser power labels. Laser power influenced to form pores or cracks determining the part quality and was positively-linearly dependent to the density of the part. Using the neural network of which the number of nodes is dropped with increasing the layer number achieved satisfactory inference when melt-pool images had blurred edges. The proposed neural network showed the classification failure rate under 1.1% for 13,200 test images and was more effective to monitor melt-pool images because it simultaneously handled various shapes, comparing with a simple calculation such as the sum of pixel intensity in melt-pool images. The classification model could be utilized to infer the location to cause the unexpected alteration of microstructures or separate the defective products non-destructively.

Keywords Additive manufacturing · Powder bed fusion · Selective laser melting · Melt-pool classification · Deep neural network

Introduction

Metal additive manufacturing (AM) using selective laser melting is an emerging technology to produce metal parts such as aerospace engine and medical implants. The process repeats two steps. First, metal powders are spread on the same metal-based build plate. Next, by scanning a laser selectively, powders are fused and solidified on the cross-section of part. Forming merely an AM part is easy, but the part quality is a different matter. The quality of AM parts is directly affected by the underlying microstructure that is a permanent characteristic of the AM process, for example, pores and cracks act to worsen the part quality

(Seifi et al. 2016). During AM process, part quality problems such as porosity, cracking, and layer delamination are caused by stochastic powder layer and melt-pool dynamics. Bauereiß et al. (2014) developed a mesoscopic numerical hydrodynamics model including capillary and wetting effects for melting process and showed that the stochastic powder layer were the origin of defect formation. Khairallah et al. (2016) also showed that strong dynamical melt flow generated pore defects, spattering, sparking, and denudation zones by using a three-dimensional high fidelity powder-scale model. Part quality problems have been typically solved by a try-and-error method which is adjusting the process parameter settings, but the fluctuation in part quality occurs despite same settings (Tapia and Elwany 2014). The causes of part quality fluctuation could be identified by monitoring in situ process phenomena as well as process or equipment parameters. In situ monitoring for powder-coated layer, build plate, melt-pool area, or melt-pool temperature is one of the key technologies that could guarantee the part quality at mass production industry, control AM process carefully and consistently, and infer the formation of microstructures without using microscopic images which are gathered by the destruction of AM parts. Especially, in situ melt-pool monitoring has been studied to develop closed-loop feedback

✉ Kangil Kim
kangil.kim.01@gmail.com

¹ Additive Manufacturing R&D Group, Gangwon Regional Division, Korea Institute of Industrial Technology, 137-41, Gwahakdanji-ro, Sacheon-myeon, Gangneung-si, Gangwon-do 25440, Republic of Korea

² WINFORSYS, 24F, U-Tower, 767, Sinsu-ro, Suji-gu, Yongin-si, Gyeonggi-do 16827, Republic of Korea

³ Computational Intelligence Lab, Department of Computer Science and Engineering, Konkuk University, 120 Neungdong-ro, Gwangjin-gu, Seoul 05029, Republic of Korea

system and minimize the fluctuation in part quality (Everton et al. 2016). Berumen et al. (2010) utilized an in-line camera system to capture the irradiation emitted by the melt-pool. Craeghs et al. (2012) developed a feedback system to control laser power by capturing melt-pool image and light intensity with a high-speed camera and photodiode. Lane et al. (2016) quantified the temperatures, heating and cooling rates in and around the melt pool by using InSb mid-wave infrared camera.

The melt-pool of selective laser melting is an interaction region between laser beam and powder. Most laser energy is rapidly absorbed by powder particles. The short time of laser irradiation causes locally melting zone, which is called the melt-pool. The temperature and shape of the melt-pool are determined by laser irradiation parameters such as laser power, laser spot size and scan speed, heat conduction among powder particles and metal build plate, and heat convection between chamber atmosphere and melting zone (Shi et al. 2016). A high-speed camera could capture the image of a melt-pool, which indirectly informs of the intensity and spatial distribution of visible light emitted from the melt-pool. Gray scale value of a high-speed camera corresponds to the intensity of the emitted light which is dependent on the temperature. The shape and the number of white pixels correspond to the heat affected zone and the width of melt-pool. By-products such as spatters, splashes, and fumes could also be present in the melt-pool image, but that image will be excluded for training and testing the network. When a final AM part is built by ten thousands of layers and over, using in situ process monitoring generates hundreds of gigabyte data and more. Images gathered by a high-speed camera, especially, also show a variety of shapes. It is impossible to classify melt-pool images by human eye perfectly or create simple model for image classification, because minimum millions of melt-pool images with various shapes are obtained at each layer. For classifying a lot of melt-pool images, machine learning method such as a deep neural network could be a potential solution.

Machine learning has started to be applied to diverse additive manufacturing areas. Xiong et al. (2014) proposed the artificial neural network to predict bead geometry for robotic Gas Metal Arc Welding (GMAW)-based rapid manufacturing. Panda et al. (2016) used the genetic algorithm to quantify and optimize process parameters in Wire Arc Additive Manufacturing (WAAM). DeCost et al. (2017) used computer vision and machine learning to characterize and classify AM powder feedstocks. Song et al. (2017) used several machine learning techniques to predict the composition such as Al concentration using laser-induced plasma spectroscopy. Mohamed et al. (2017) studied the relationship between process parameters and creep performance of fused deposition modeling parts. Zhang et al. (2017) used the genetic algorithm to search for an optimal combination

of AM part build orientations to minimize the total build time and cost at a global optimal level. Aminzadeh and Kurfess (2018) created a database of camera images from every layer of AM parts and used the Bayesian classification model to detect layers or sub-regions with low quality of fusion or defects. Garg et al. (2018) improved the part properties such as surface roughness, waviness, tensile strength, dimensional accuracy by using the genetic algorithm. The former researches mainly focused on how to optimize AM process parameters by using machine learning, but no work to study melt-pool images during AM process with machine learning has been found in literature. Therefore, the main purpose of this study on selective laser melting (SLM) process monitoring is to propose a deep neural network to classify melt-pool images obtained during SLM process with respect to the laser power.

In artificial intelligence history, a deep neural network is not new at all and there are a variety of classifiers developed on statistical and optimization theories as Support Vector Machine (SVM) (Cristianini and Shawe-Taylor 2000), Bayesian network (Conrady and Jouffe 2015), Markov Random Field (Li 1994), Decision Trees (Rokach and Maimon 2014), Rule-based systems (Jackson 1998). Main potential of deep neural networks compared to the other models is to learn probabilistic and structural information without bias generated by incomplete expert knowledge and implicit restriction of algorithms. For example, selecting important features in SVM and building a dependency structure in Bayesian network should be manually designed. There exist searching methods to find an optimum for such structural information, but they usually require huge-computational cost and therefore are restricted to succeed in solving real-world problems. Neural networks also have this problem, but their integrated framework could overcome the issue with strong computing power and huge amount of data. This property does not necessarily imply that other models are impossible in solving target applications. It rather implies that deep neural networks could easily and quickly obtain a good performing model while the other models may take enormous time of designing structures and features based on human knowledge. Among various machine learning method, deep learning using artificial neural network with hidden layers has shown excellent performance for regression and classification of big image data (Krizhevsky et al. 2012; Sun et al. 2013). Existing definitions to deep learning are summarized into 4 definitions, and the deep learning used in this study is defined that a class of machine learning algorithms using a cascade of multiple layers of nonlinear functions for feature extraction, which is similar definition 4 of the reference (Zhang et al. 2018).

There have been a surge of applications using deep neural networks, which uses the stacked and layer-wised fully connected network structure. This intelligence algorithm is equal to multilayered perceptron which widely spread out

near 1990s (Haykin 1998) except using very deep layered structure. In the last decade, many initialization and training techniques (Bengio et al. 1994; Hinton et al. 2006; Ioffe and Szegedy 2015) have been developed and very deep structures could be finally trained with breakthrough on computing power using GPUs. Learning deep structure led to solving practically complex problems as image classification (Ren et al. 2017), showing better prediction accuracy than human. For the past three years, many researches also have adopted machine learning to solve problems in the manufacturing industry. Pashazadeh et al. (2016) estimated welding formation quality from welding parameters such as welding current and voltage, welding pressure by using the artificial neural network. Abhishek et al. (2017) has focused on optimizing the cutting quality such as material removal rate, surface roughness, or cutting force and predicting life time of a tool by training the artificial neural network. Tsai and Luo (2017) combined the artificial neural network with a genetic algorithm to optimize injection molding parameters for the accuracy of optical lens form. Zhao et al. (2017) developed an apparel design system to satisfy the customer's increased demand for apparel products in the aspect of function and emotion by using the artificial neural network. Furthermore, vision research with the artificial neural network like this study also has been conducted to develop the prediction and classification model. You et al. (2015) proposed an artificial neural network to predict the geometrical parameters and detect welded defects by using optical features which were obtained by ultraviolet visual sensor, auxiliary illumination visual sensor, and X-ray visual sensor. D'Addona et al. (2017) employed the artificial neural network to predict the degree of tool-wear from tool-wear images. Machine vision technology were also often adopted in molding process and electrical component manufacturing because manual inspection often missed a crack or a void. Librantz et al. (2017) proposed the method to evaluate and inspect molds surfaces

by using artificial neural network and the laser light scattered image processing. Sun et al. (2016) proposed the system that incorporated machine vision with the artificial neural network to inspect defects of thermal fuses.

Our application to model relations between melt-pool images and laser powers could be interpreted as an image classification problem and therefore we designed a deep neural network to obtain state-of-the-art results as vision research literature, collecting rich-data and supporting high-performance computing environment. Information about equipment gathering melt-pool images, AM process parameters, and workflow for training, validating, testing of deep neural network were described in “Experiment design” and “Deep neural network design” section. Microscopic images of metal AM parts, parametric study of the neural networks in “Results” section. The classification performance and discussion about the neural network and applications of melt-pool images were presented in “Discussion” section. The final section is a conclusion.

Experiment design

This study used the melt-pool monitoring system of selective laser melting which was developed by WINFORSYS (Fig. 1). Melt-pool monitoring system gathered melt-pool images along the path where laser is rapidly irradiated. The melt-pool monitoring system was composed of a dichroic mirror, a galvanometer scanner, an F-theta lens, and a high-speed camera. The system used a continuous wave fiber laser of 1075 nm. The focused laser beam of 100 μm was reflected by the dichroic mirror and positioned by galvanometer scanner. The dichroic mirror spectrally separated light by reflecting and transmitting light as a function of wavelength. Laser wavelength was reflected, and visible wavelength from 450 nm to 900 nm was transmitted through the dichroic

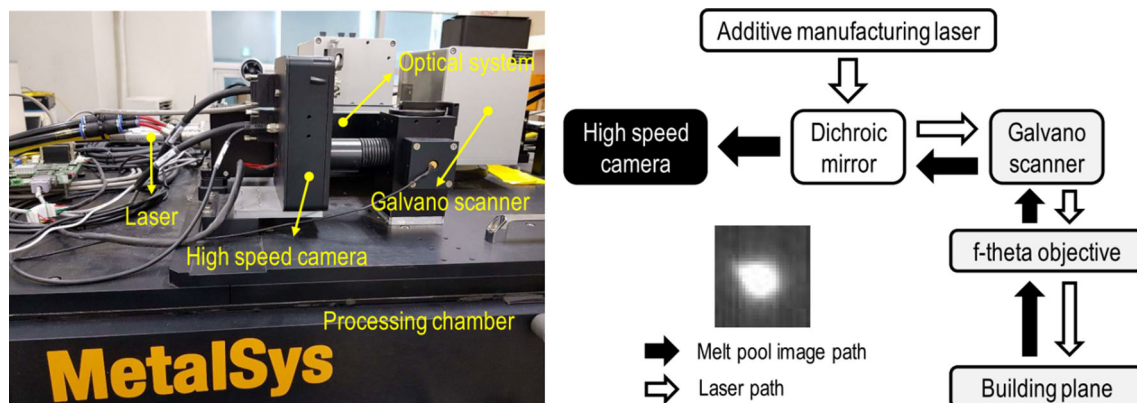


Fig. 1 Melt-pool monitoring system of selective laser melting which was developed by WINFORSYS

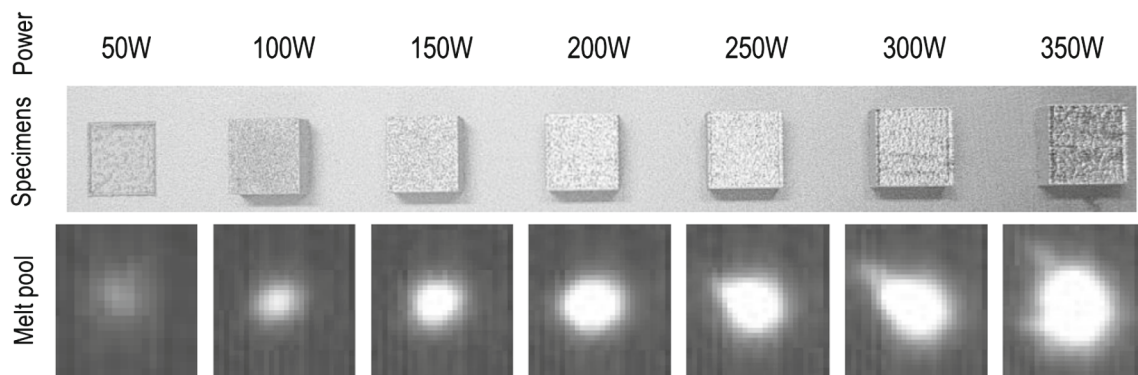


Fig. 2 SUS316L-based specimens and melt-pool images for each laser power condition

mirror used in this experiment. The laser beam through the F-theta lens heated powder particles and formed the melt-pool. The light from the melt-pool was irradiated hemispherically, and the only co-axial light at the galvanometer mirror was transmitted through the F-theta lens, the scanner, and the dichroic mirror. Finally, the light of visible wavelength arrived at the high-speed camera. The high-speed camera of 1.3 M resolutions and 8bit gray scale was connected to the data acquisition board with serial communication. The data acquisition system gathered the cropped images of 512×512 pixels at framerates of 2.5 kHz. An Field Programmable Gate Array (FPGA) chip was used to gather and manipulate the image data. If the system to capture melt-pool images and the system to save the location of that image work separately, the time error between two systems may occur. The data acquisition system simultaneously gathered a melt-pool image and a location information in real time. The location information of x- and y-coordinate was converted to two binary numbers of 8bit, and those binary numbers were inserted at insignificant pixels of the upper left corner of a melt-pool image. The details of the data acquisition equipment and method are described in the patent of WINFORSYS (Cho et al. 2017).

7 specimens were produced on the same SUS316L-based build plate at the same time. Process parameters of all specimens were same except laser power. Hatching distance was set on 100 μm . Scan speed was fixed at 2.5 m/s. Each specimen had 8.5 mm in depth, 8.5 mm in width, and 4 mm in height (Fig. 2), and was built with 150 layers. Laser powers were set on 50, 100, 150, 200, 250, 300, and 350 W. The sample of 50 W laser power was not built at all, and melt-pool images of 50 W laser power were not utilized to train the neural network. SUS316L powders having D50 of 28.5 μm were used. Layer thickness was set on 30 μm . Hatching strategy was the stripe pattern, and it rotated through 67 degrees for each layer. Process gas was argon, and oxygen density was controlled under 0.1%. The microstructure images of specimens were captured by the optical micro-

scope (VHX-5000, KEYENCE). The microstructure images were used to observe pores or cracks and quantify the part density. The density is one of the important characteristics to determine the performance of the part, for example, high density is determined by how many pores are not present. The density is generally derived by Archimedes' principle or micro-computed tomography, but in this study, it was derived by thresholding algorithm of image segmentation method. At first, color microstructure images were converted to gray-scale images for calculating the densities. Using thresholding algorithm changed a gray-scale image to a binary image such as black (0) and white (255) based on a threshold value. For example, when a threshold value is 125, pixels over 125 are set to 255 and pixels under 125 are set to 0. Finally, the density was obtained by averaging the ratio of the number of white pixels to the number of whole pixels for 10 microstructure images. The threshold value was determined as follows: (1) Calculate all densities of one image when varying a threshold value from 0 to 255. Increasing a threshold value lowers a density because the number of white (255) pixels also decreases, but in the certain ranges, the density slowly changes. (2) Calculate the derivative of a density function with respect to a threshold value. (3) Find the threshold value at which the minimum of the derivative of a density function occurs. The threshold value at the derivative minimum indicates the most insensitive point to the change of the threshold value. Therefore, this threshold could generate two groups of pixel intensity which are the most robust to the density error caused by discretizing the intensities of pixels.

For 6 laser power conditions from 100 to 350 W, gathering melt-pool images started at the 50th layer and ended at the 99th layer. When the laser was irradiated along the programmed path, melt-pool images were captured with the framerate of 2.5 kHz and were saved in the data acquisition system. The image was clipped into 60×60 pixels because the luminous region is about 5% of whole area of the original image. The acquired images were raw data, and included

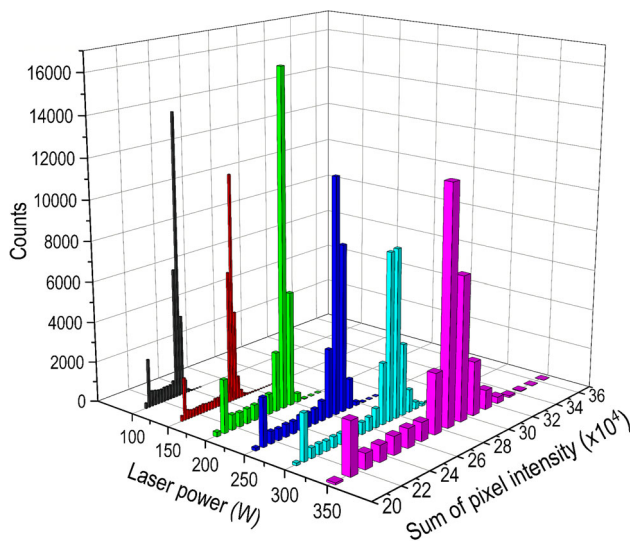


Fig. 3 Histograms of ‘the sum of pixel intensity’ of total acquired images for 6 laser power conditions

abnormal images such as blurs, fumes, or a blank image. Pre-processing of images was used to filter noise images. First, the sum of whole pixel intensity of each image was calculated and used to make a histogram for each laser power condition. Figure 3 shows histograms of ‘the sum of pixel intensity’ of total acquired images for 6 laser power conditions. Images among intervals of which the number of counts was over 2000 were defined as to be normal in this study, which were distributed among only 3 or 4 intervals. This criterion was empirically determined to accept as various melt-pool images as possible. Although some intervals of which the sum of pixel intensity were under 220,000 also had 2000 counts over, all images in those intervals were noise images. Table 1 shows the intervals of the sum of pixel intensity which corresponded to the criteria of the normal image and the ratios of normal images to total acquired images for 6 laser power conditions. We used 67–75% of total acquired images to develop the neural network, and finally, total number of images used for training, validation, and test was randomly adjusted to 22,000 per a laser power condition.

Table 1 The intervals of the sum of pixel intensity which corresponded to the criteria of the normal image and the ratios of normal images to total acquired images for 6 laser power conditions

Power (W)	Criterion of the normal image (sum of pixel intensity, $\times 10^4$)	# of normal images (A)	# of total acquired images (B)	Ratio of A to B (%)
100	22.8–23.4	24,436	33,793	72.3
150	24.0–24.6	22,136	33,087	66.9
200	24.5–26.0	25,036	33,193	75.4
250	25.5–27.0	23,201	33,091	70.1
300	26.5–28.5	23,118	33,194	69.6
350	27.0–31.0	24,568	33,115	74.2

Deep neural network design

One melt-pool image was labeled the laser power of input settings. 22,000 melt-pool images formed by 1 laser power were labeled the same value. The purpose of the neural network is classifying a melt-pool image with respect to a laser power. Figure 4 shows the frame of a feedforward artificial neural network with several hidden layers and fully connected nodes. For the input layer, the pixel intensities of 60×60 array were transformed into 1×3600 array, and were standardized as follows:

$$x'_i = \frac{x_i - \mu}{\sigma} \quad (1)$$

x'_i is a standardized pixel intensity. x_i is an original pixel intensity. μ and σ are mean value and standard deviation of whole pixel intensities in an image. The network included L hidden layers, which were composed of L weight matrices $\mathbf{W} = \{\mathbf{W}_1, \dots, \mathbf{W}_L\}$ and L bias matrices $\mathbf{b}_1, \dots, \mathbf{b}_L$. The weighted sum at l th layer \mathbf{Z}_l was determined by an inner product of the weight at l th layer \mathbf{W}_l and the output from a previous layer \mathbf{A}_{l-1} plus the bias at l th layer \mathbf{b}_l . After applying batch normalization (Goodfellow et al. 2016) to \mathbf{Z}_l for regularization, ReLU (Goodfellow et al. 2016) was used as the activation function and final output at l th layer was \mathbf{A}_l . The inference value p was determined by an inner product of the weight \mathbf{W}_L and the output from $(L - 1)$ th hidden layer \mathbf{A}_{L-1} plus the bias at L th hidden layer \mathbf{b}_L . He’s method (Goodfellow et al. 2016) for weight initialization was used. To train the neural network, we used AdaDelta method (Zeiler 2012), which is a gradient-based optimizer using second derivative known as momentum. After evaluating gradient and momentum of one model, this method updates model parameters. In practical implementation, this method uses dynamic programming to evaluate the gradient and hessian, storing partial evaluation results. This implementation is exactly equal to backpropagation (Goodfellow et al. 2016).

Figure 5 shows flowcharts which explain how a deep neural network was trained to predict the laser power for each

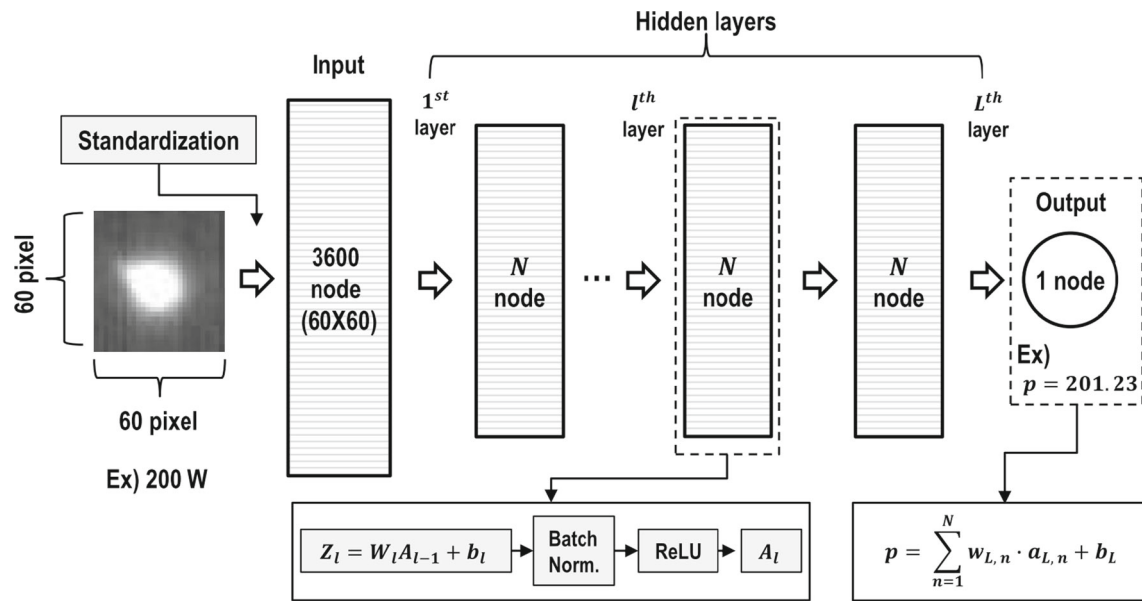


Fig. 4 Frame of a feedforward artificial neural network with several hidden layers and fully connected neurons

melt-pool image and how the classification performance of the neural network was evaluated. At first, the network f randomly estimated output h_{ij} using the label for training y_{ij} and the melt-pool image for training x_{ij} . i corresponds to 6 laser power conditions, j corresponds to the number of images, i.e. 17,600 training images per a laser power condition. After that, the cost function, Mean Squared Error (MSE) was calculated as follows:

$$\text{MSE} = \frac{1}{N} \sum_{k=1}^N (y_k - h_k)^2 \quad (2)$$

N is the number of all images for each purpose such as training, validation, or test. Using the back-propagation algorithm (Goodfellow et al. 2016) found the proper W and b to minimize MSE. This computation was a process to train the network and was repeated till overfitting occurred. Unknown 2200 validation images per a laser power condition were used to detect overfitting and validating the network. The overfitting was decided when MSE of the validation images set started to be higher than training images. It means that the estimation is highly accurate in only training images, not unknown images. Early stopping algorithm (Goodfellow et al. 2016) was used to detect the overfitting and save the best weights. The patience value of early stopping algorithm was 5000 epochs. The finally saved neural network g evaluated its accuracy and regression performance using another unknown test images different from validation images. MSE in 2200 test images per a laser power condition was used to evaluate the accuracy of the network. Regression coefficient R between 13,200 labels and 13,200 estimated laser pow-

ers of test images was also used to evaluate the regression performance of the network. Regression coefficient R was calculated as follows:

$$R = \frac{\sum_{k=1}^{13,200} (y_k - \mu_y)(h_k - \mu_h)}{\sum_{k=1}^{13,200} (y_k - \mu_y)^2} \quad (3)$$

μ_y is the mean of all labels, and μ_h is the mean value of all predicted outputs. If R is close to 1, the estimated value is close to the exact laser power. The accuracy and regression performance of the network were varied by the number of the hidden layers and nodes and those results are described in “Results” section.

Results

The microstructure images were observed to understand how additive manufactured parts were influenced by the laser power. Figure 6 shows the cross-sectional microstructure images of the specimens along a building direction. The lower side of the image means that it was deposited earlier than the upper side of the image. When insufficient laser power such as 100 W, 150 W, and 200 W was irradiated on powder particles, non-spherical pores were created. These pores were caused by un-melted or partially-melted powder particles. When the laser power was higher than 250 W, pores were reduced drastically. The sample of 50 W laser power was not built at all. Table 2 shows the increase of the density as laser power increases. The shapes of the melt-pools were also varied by the laser power (Fig. 2). A pixel area corresponds to $20 \times 20 \mu\text{m}^2$ on the build plate, and the width of

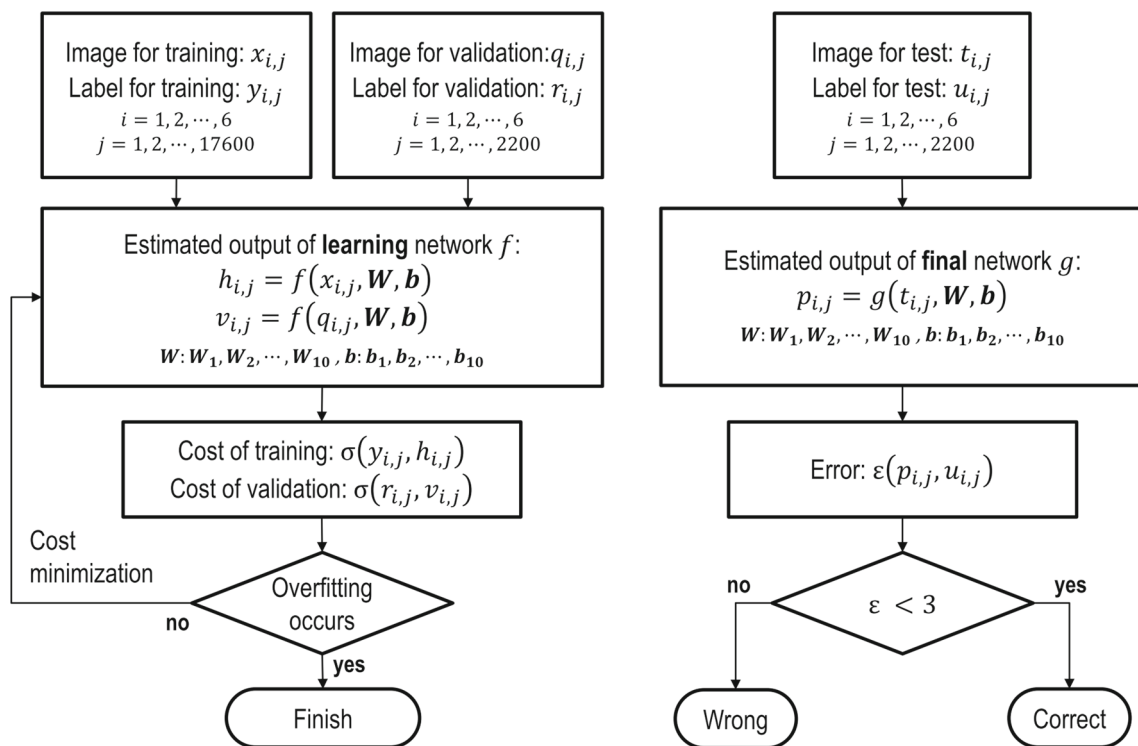


Fig. 5 Flowcharts to train the deep neural network for classifying melt-pool images by laser powers, and to calculate the error rate of the trained network

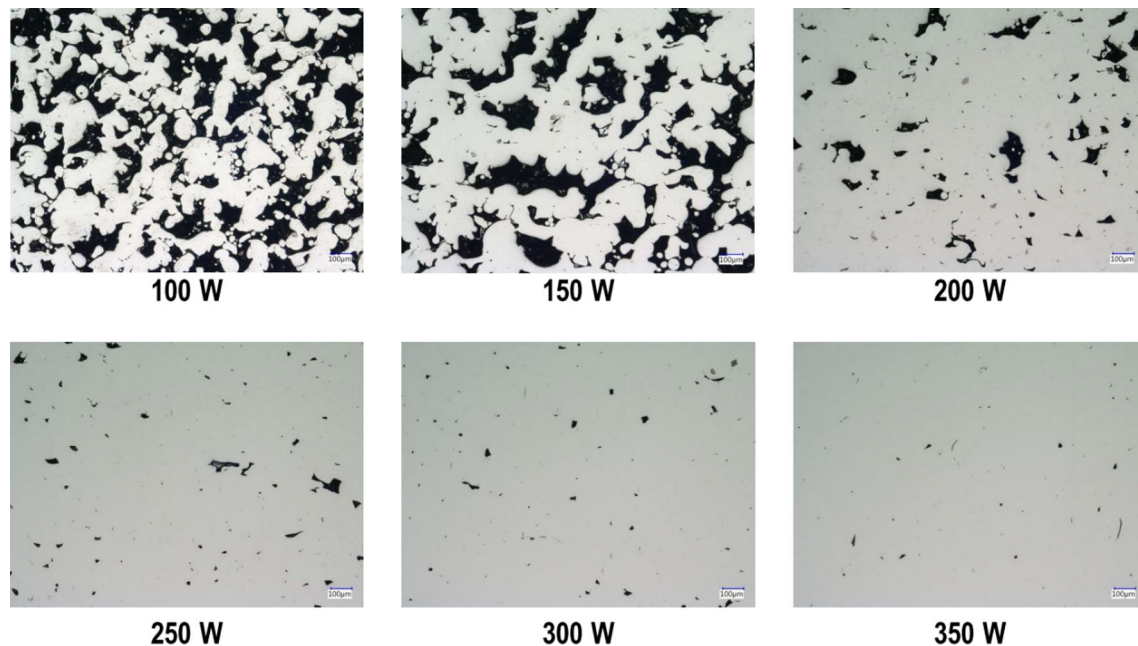


Fig. 6 Microstructure images of specimens for each laser power condition (Scale bar is 100 μm)

a melt-pool could be approximately calculated from a melt-pool image. Table 2 also shows the width of a melt-pool for each laser power. The width of melt-pool was between 100 and 500 μm. As the laser power increased, the luminous area of the melt-pool image was enlarged. When the laser

power was under 100 W, the maximum intensity of melt-pool was not fully white. When the laser power over 250 W was applied, a faint tail caused by high energy and moving laser were appeared. Increasing laser power transferred more energy to powder particles, expanded the heat-affected zone,

Table 2 Density of specimens and width of a melt-pool for each laser power

Power (W)	50	100	150	200	250	300	350
Density (%)	–	63.25	81.97	95.30	98.98	99.51	99.77
Width (μm)	100	160	240	280	300	380	460

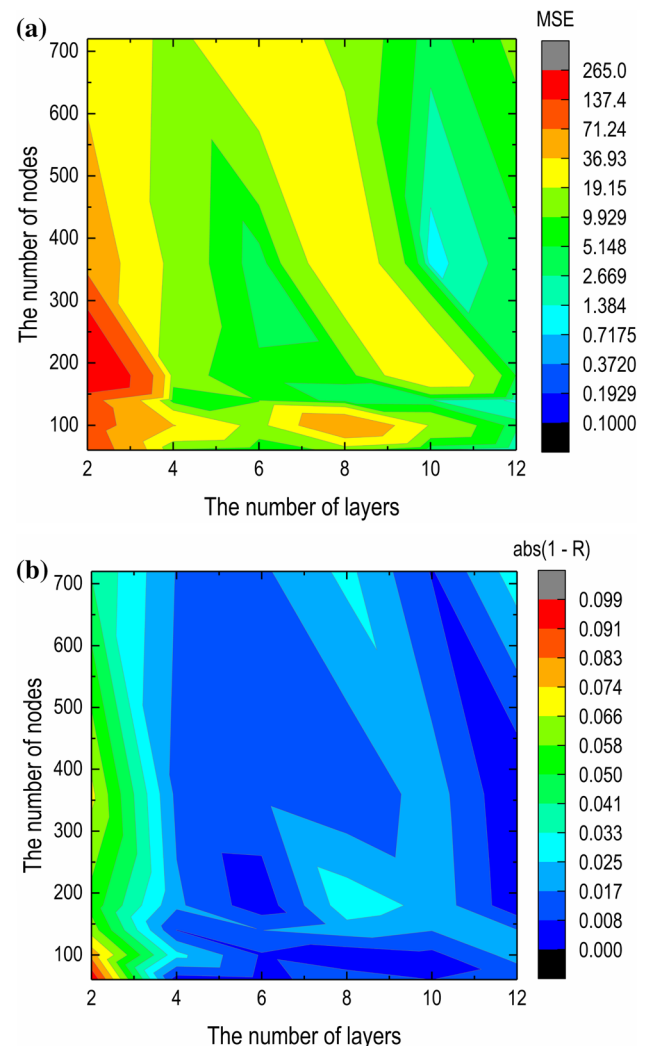
reduced pores produced by the un-melted or partially-melted zone, and increased the density of the specimen.

Varying the number of hidden layers and nodes, the neural networks for classification of melt-pool images were trained. MSE and R of test images were used to determine the proper numbers of hidden layers and nodes for predicting the laser power, and the accuracy and the regression performance of the neural network corresponded to MSE and R . The number of hidden layers was selected such as of 2, 4, 6, 8, 10, 12, and the number of nodes was selected such as 60, 100, 140, 180, 360, 720. Each layer of hidden layers had the same number of nodes. We used a single Nvidia GTX 1080Ti GPU for training the neural network, and in this system, the case of 10 and 12 hidden layers required 5.6 s and 5.7 s to train the model for one epoch, but the case of 14 and 16 hidden layers required 6.8 s and 7.6 s. After 14 hidden layers, increasing the number of layers spent more time on training the model. Therefore, we chose 12 as the upper limit of hidden layers due to trade-off according to the system performance. Figure 7 shows MSE and the absolute value of $1 - R$ for all combination of hidden layers and nodes. MSE of 2 hidden layers neural network was the highest at any node condition. The minimum of MSE occurred at 10 hidden layers neural network with 360 nodes. Increasing the hidden layer reduced MSE except 8 hidden layers neural network. However, the absolute values of $1 - R$ in most neural network were similar except 2 hidden layers neural network. R values of 2 hidden layers neural network were the farthest to 1. MSE and R were more sensitive to the variation of the number of hidden layers and robust in the variation of the number of nodes.

Training the neural networks of which the number of nodes dropped with the layer number, MSE and R of those neural networks in test images were also computed to compare with the neural network of which the number of nodes was fixed at all layers. When the number of hidden layers was chosen 10, the nodes were dropped by the function n as follows:

$$n = 3600 \cdot m^k \quad (4)$$

m decreases from 0.9 to 0.1 with the increase of the layer number from 1 to 9. The layer number 0 was input layer, and 10 was output layer. k was selected such as 1, 2, 3. Table 3 shows the number of nodes for each hidden layer by varying k value, and Table 4 shows MSE and R in test images for the neural network of which the number of nodes dropped by varying k value. Increasing k dropped the number of nodes

**Fig. 7** **a** MSE and **b** the absolute value of $1 - R$ for all combination of hidden layers and nodes

more rapidly with the layer number. In the case of the neural network of k value of 2, MSE was the lowest, and R was robust in the variation of k value and was closer to 1 than 10 hidden layers neural network which nodes were fixed at all layers.

Discussion

In this section, the classification performances of the melt-pool images were evaluated for two models, 10 hidden layers

Table 3 The number of nodes for each hidden layer by varying k value of the equation $n = 3600 \cdot m^k$

Layer m	0 (Input)	1 0.9	2 0.8	3 0.7	4 0.6	5 0.5	6 0.4	7 0.3	8 0.2	9 0.1	10 (Output)
$k = 1$	3600	3240	2880	2520	2160	1800	1440	1080	720	360	1
$k = 2$	3600	2916	2304	1764	1296	900	576	324	144	36	1
$k = 3$	3600	2624	1843	1235	778	450	230	97	29	4	1

Table 4 MSE and R in test set for the neural network of which the number of nodes drops by varying k value of the equation $n = 3600 \cdot m^k$

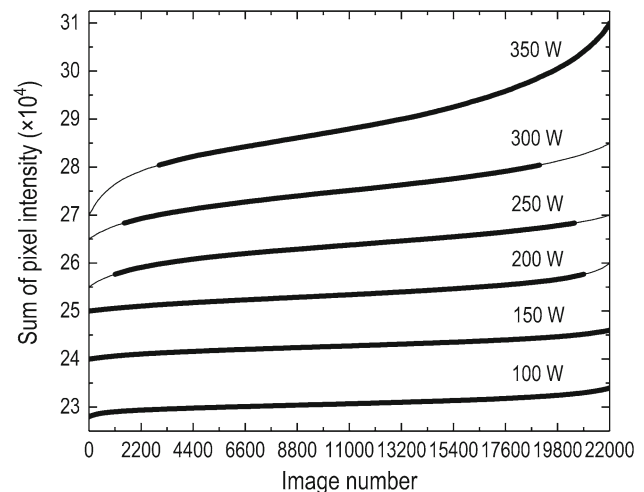
	$k = 1$	$k = 2$	$k = 3$
MSE	21.50	1.29	22.35
R	1.003	0.996	0.999

neural network with 360 nodes at all layers (10HL-360NA) and 10 hidden layers neural network of which the number of nodes was dropped by Eq. (4) with k value of 2 (10HL-DNK2). Before the comparison, the classification method currently used in WINFORSYS will be described. WINFORSYS has used a simple and general method to classify melt-pool images by means of calculating only the sum of pixel intensity, and it is inaccurate. Figure 8 shows the sum of pixel intensity in 22,000 images for each laser power. Images were sorted by the sum of pixel intensity. Solid line represents the range of images to be classified perfectly, but thin line represents the range of images not to be classified at all. Classifying melt-pool images of 100, 150 W was ‘trivial’ because any images were not overlapped. In the condition of 200 W and more, however, some images of thin line were overlapped with the other condition. Table 5 shows the classification failure rate of ‘sum of pixel intensity method’. The classification failure rate in this method was defined as a ratio of the number of images to fail the classification successfully to the number of total images. The classification failure rate increased in the condition of 200 W and more laser power. Therefore, using the sum of pixel intensity was not suitable method to classify melt-pool images.

The classification performances of 10HL-360NA and 10HL-DNK2 were evaluated by the classification failure rate which was a ratio the number of images to be out of the correct inference range to total number of images (17,600 images for training + 2200 images for validation + 2200 images for test = 22,000 images) per a laser power using tenfold cross-validation (Goodfellow et al. 2016). The correct inference range was defined as follows:

$$\varepsilon = \frac{|p_{i,j} - u_{i,j}|}{u_{i,j}} \times 100 < 3 \quad (5)$$

$u_{i,j}$ corresponds to the label (input laser power) of a test image, and $p_{i,j}$ corresponds to the estimated laser power using

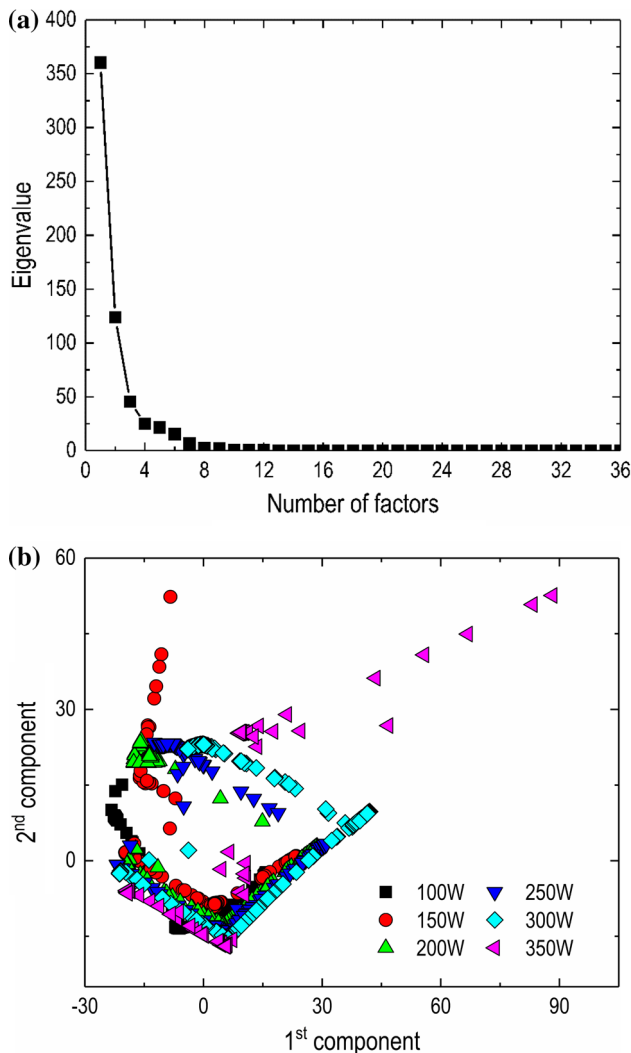
**Fig. 8** Distribution of melt-pool images derived by means of calculating the sum of pixel intensity in 22,000 images for each laser power (Images were sorted by sum of intensity)**Table 5** Classification failure rates for 22,000 images per a laser power which are derived by three methods such as using ‘sum of pixel intensity’ method, 10 hidden layers neural network with 360 nodes at all layers (10HL-360NA), and 10 hidden layers neural network of which the number of nodes is dropped by equation $n = 3600 \cdot m^k$ with k value of 2 (10HL-DNK2)

Power (W)	100	150	200	250	300	350
Classification failure rate (%)						
‘Sum of pixel intensity’	0	0	5.00	11.79	20.24	13.47
10HL-360NA	80.10	28.85	0.52	16.83	0.09	0.2
10HL-DNK2	1.11	0.41	0.01	0.1	0.02	0.09

the final neural network g . When the error ε was under 3, it was judged the correct classification. The criterion for judgement comes from maximum long-term power instability of laser generator (YLR-AC 400W Datasheet 2018) because the range of power instability in a real device is commonly allowed by the equipment maker. Table 5 shows the averaged classification failure rates of 10HL-360NA and 10HL-DNK2 for each laser power. 10HL-360NA showed an improving trend of the classification failure rate as the laser power increased. The classification failure rate of 100 W was particularly high compared with other laser power conditions.

Table 6 leave-one-out (LOO) evaluation result of 10HL-DNK2 for all laser powers

Leaved (W)	Label (W)					
	100	150	200	250	300	350
100	291.03	150.01	201.01	251.03	300.04	350.66
150	102.46	193.39	199.22	251.00	301.82	350.18
200	100.76	153.50	131.79	250.52	298.73	349.76
250	100.81	154.46	193.40	191.64	299.33	350.01
300	101.74	149.70	200.11	249.01	349.06	349.66
350	99.84	150.09	200.05	249.30	300.68	265.41

**Fig. 9** **a** Scree plot and **b** first-two principal component score plot for 36 nodes (features) of the last layer of 10HL-DNK2 when 2200 test images per a laser power condition were inputted

Using the neural network of which the number of nodes was fixed at all layers worsened the classification performance when melt-pool images had blurred edges. However, 10HL-DNK2 showed steady and more improved performance of the classification, of which the classification failure rate was

under 1.1% for 13,200 test images. 10HL-DNK2 also showed that classification failure rate worsened when the laser power was under 150 W, but those value were low compared with 10HL-360NA. Using the neural network of which the number of nodes was dropped with increasing the layer number achieved satisfactory inference ability despite blurred edges.

Leave-one-out (LOO) evaluation is another method to analyze the inference ability of 10HL-DNK2. The procedure of LOO evaluation was to train the neural network with training images of 5 laser power conditions except 1 condition and after that, to test the neural network with test images of 6 laser power conditions including the omitted condition. The number of training images and test images were 17,600 and 2200 per a laser power condition. This procedure repeated until all the conditions served as test cases on the LOO evaluation. Table 6 shows the LOO evaluation result of 10HL-DNK2. The diagonal values of Table 6 corresponded to the LOO evaluation results. The estimated laser power values in the case normally training with their training images was within the correct inference range. However, the case of LOO evaluation got abnormal estimated laser power values. Especially, the difference between the label and the estimated value at 100 and 350 W was higher than other laser power conditions. We recognize that the proposed neural network could be used as a classifier rather than a regression. Gathering melt-pool images in more input conditions may increase the accuracy of LOO evaluation result, but the resolution of the camera, at the same time, also needs to be improved to distinguish images among close laser power conditions.

Principal component analysis (PCA) was used to visualize the clusters of melt-pool images classified by 10HL-DNK2. PCA is a well-known method to reduce the dimensionality for high-dimensional datasets and used to visualize clusters of the original data. Figure 9 shows scree plot and first-two principal component score plot for 36 nodes (features) of the last layer of 10HL-DNK2 when 2200 test images per a laser power condition were inputted. Scree plot suggested number five factors as the point where the slope clearly levels off. The sum from first factor to fifth factor of eigenvalues was over 95% of the sum of all variances (eigenvalues). The first-two principal component score plot hardly distinguished

each laser power condition because first-two principal components were insufficient to explain the difference among melt-pool images of 6 laser power conditions.

As mentioned earlier, the co-working equipment maker has used a simple calculation such as the sum of pixel intensity in melt-pool images to monitor AM process. This typical method is unsuitable for classifying melt-pool images because a variety of melt-pool shapes are neglected. The neural network of which the number of nodes dropped with increasing the layer number is effective to classify melt-pool images because it simultaneously handles various shapes. When the estimated laser power at a certain location is out of the correct inference range, we could identify where abnormal process occurs. We also expect that this technique could be applied to closed-loop feedback system for controlling the laser power.

Conclusion

The classification model of melt-pool images with respect to the laser power was studied through manipulating deep neural networks, and it was understood that microstructures of the part were influenced by the laser power which is positively-linearly dependent to the density of the part. Parametric study of the neural networks indicated that MSE and R were more sensitive to the variation of the number of hidden layers and robust in the variation of the number of nodes. Using the neural network of which the number of nodes was fixed at all layers worsened the classification performance, but using the neural network of which the number of nodes was dropped with increasing the layer number achieved satisfactory inference when melt-pool images had blurred edges. The better-performed neural network (10HL-DNK2) was more effective to monitor melt-pool images because it simultaneously handled various shapes compared with a simple calculation such as the sum of pixel intensity in melt-pool images. However, the proposed neural network was only used as a classifier rather than a regression model because it had weak performance on the LOO evaluation. Nonetheless, we expect that the quantification of melt-pool images using the proposed neural network could be utilized to determine whether AM process state is normal or abnormal and to separate the defective products non-destructively.

Acknowledgement This work was supported by the Korea Institute of Industrial Technology as “Development of high efficient production technology for high purity titanium powder and additive manufacturing processing technology (KITECH EO-18-0012)”.

References

Abhishek, K., Kumar, V. R., Datta, S., & Mahapatra, S. S. (2017). Parametric appraisal and optimization in machining of CFRP

- composites by using TLBO (Teaching Learning Based Optimization algorithm). *Journal of Intelligent Manufacturing*, 28(8), 1769–1785.
- Aminzadeh, M., & Kurfess, T. R. (2018). Online quality inspection using Bayesian classification in powder-bed additive manufacturing from high-resolution visual camera images. *Journal of Intelligent Manufacturing*. <https://doi.org/10.1007/s10845-018-1412-0>.
- Bauereiß, A., Scharowsky, T., & Körner, C. (2014). Defect generation and propagation mechanism during additive manufacturing by selective beam melting. *Journal of Materials Processing Technology*, 214(11), 2522–2528.
- Bengio, Y., Simard, P., & Frasconi, P. (1994). Learning long-term dependencies with gradient descent is difficult. *IEEE Transactions on Neural Networks*, 5(2), 157–166.
- Berumen, S., Bechmann, F., Lindner, S., Kruth, J.-P., & Craeghs, T. (2010). Quality control of laser- and powder bed-based Additive Manufacturing (AM) technologies. *Physics Procedia*, 5(13), 617–622.
- Cho, J.-H., Kim, M.-S., & Ji, S.-Y. (2017). Apparatus for recording location of forming in 3D printer and 3D printer having the same. KR Patent 10-1793573, 3 Nov 2017.
- Conrady, S., & Jouffe, L. (2015). *Bayesian networks and bayesialab—A practical introduction for researchers*. Franklin: Bayesia USA.
- Craeghs, T., Clijsters, S., Kruth, J.-P., Bechmann, F., & Ebert, M.-C. (2012). Detection of process failures in layerwise laser melting with optical process monitoring. *Physics Procedia*, 39, 753–759.
- Cristianini, N., & Shawe-Taylor, J. (2000). *An introduction to support vector machines: And other kernel-based learning methods*. New York: Cambridge University Press.
- D’Addona, D. M., Ullah, A. M. M. S., & Matarazzo, D. (2017). Tool-wear prediction and pattern-recognition using artificial neural network and DNA-based computing. *Journal of Intelligent Manufacturing*, 28(6), 1285–1301.
- DeCost, B. L., Jain, H., Rollett, A. D., & Holm, E. A. (2017). Computer vision and machine learning for autonomous characterization of AM powder feedstocks. *JOM Journal of the Minerals Metals and Materials Society*, 69(3), 456–465.
- Everton, S. K., Hirsch, M., Stavroulakis, P., Leach, R. K., & Clare, A. T. (2016). Review of in situ process monitoring and in situ metrology for metal additive manufacturing. *Materials and Design*, 95(5), 431–445.
- Garg, A., Lam, J. S. L., & Savalani, M. M. (2018). Laser power based surface characteristics models for 3-D printing process. *Journal of Intelligent Manufacturing*, 29(6), 1191–1202.
- Goodfellow, I., Bengio, Y., & Courville, A. (2016). *Deep learning*. Cambridge: The MIT Press.
- Haykin, S. (1998). *Neural networks: A comprehensive foundation*. Upper Saddle River: Prentice Hall.
- Hinton, G., Osindero, S., & Teh, Y. (2006). A fast learning algorithm for deep belief nets. *Neural Computation*, 18(7), 1527–1554.
- Ioffe, S., & Szegedy, C. (2015). Batch normalization: Accelerating deep network training by reducing internal covariate shift. *CoRR*, <http://arxiv.org/abs/1502.03167>.
- Jackson, P. (1998). *Introduction to expert systems*. Boston: Addison-Wesley Pub. Co.
- Khairallah, S. A., Anderson, A. T., Rubenchik, A., & King, W. E. (2016). Laser powder-bed fusion additive manufacturing: Physics of complex melt flow and formation mechanisms of pores, spatter, and denudation zones. *Acta Materialia*, 108, 36–45.
- Krizhevsky, A., Sutskever, I., & Hinton, G. E. (2012). ImageNet classification with deep convolutional neural networks. In *NIPS’12 proceedings of the 25th international conference on neural information processing systems* (Vol. 1, pp. 1097–1105).

- Lane, B., Moylan, S., Whittenton, E., & Ma, L. (2016). Thermographic measurements of the commercial laser powder bed fusion process at NIST. *Rapid Prototyping Journal*, 22(5), 778–787.
- Li, S. Z. (1994). Markov random field models in computer vision. *European Conference on Computer Vision*, 1994, 361–370.
- Librantz, A. F. H., de Araujo, S. A., Alves, W. A. L., Belan, P. A., Mesquita, R. A., & Selvatici, A. H. P. (2017). Artificial intelligence based system to improve the inspection of plastic mould surfaces. *Journal of Intelligent Manufacturing*, 28(1), 181–190.
- Mohamed, O. A., Masood, S. H., & Bhowmik, J. L. (2017). Influence of processing parameters on creep and recovery behavior of FDM manufactured part using definitive screening design and ANN. *Rapid Prototyping Journal*, 23(6), 998–1010.
- Panda, B., Shankhwar, K., Garg, A., & Savalani, M. M. (2016). Evaluation of genetic programming-based models for simulating bead dimensions in wire and arc additive manufacturing. *Journal of Intelligent Manufacturing*. <https://doi.org/10.1007/s10845-016-1282-2>.
- Pashazadeh, H., Gheisari, Y., & Hamed, M. (2016). Statistical modeling and optimization of resistance spot welding process parameters using neural networks and multi-objective genetic algorithm. *Journal of Intelligent Manufacturing*, 27(3), 549–559.
- Ren, S., He, K., Girshick, R., & Sun, J. (2017). Faster R-CNN: Towards real-time object detection with region proposal networks. *IEEE Transactions on Pattern Analysis and Machine Intelligence*, 39(6), 1137–1149.
- Rokach, L., & Maimon, O. Z. (2014). *Data mining with decision trees: Theory and applications*. River Edge: World Scientific Publishing Co.
- Seifi, M., Salem, A., Beuth, J., Harrysson, O., & Lewandowski, J. J. (2016). Overview of materials qualification needs for metal additive manufacturing. *JOM Journal of the Minerals Metals and Materials Society*, 68(3), 747–764.
- Shi, Q., Gu, D., Xia, M., Cao, S., & Rong, T. (2016). Effects of laser processing parameters on thermal behavior and melting/solidification mechanism during selective laser melting of TiC/Inconel 718 composites. *Optics & Laser Technology*, 84, 9–22.
- Song, L., Huang, W., Han, X., & Mazumder, J. (2017). Doubly fed induction generator system resonance active damping through stator virtual impedance. *IEEE Transactions on Industrial Electronics*, 64(1), 633–642.
- Sun, T.-H., Tien, F.-C., Tien, F.-C., & Kuo, R.-J. (2016). Automated thermal fuse inspection using machine vision and artificial neural networks. *Journal of Intelligent Manufacturing*, 27(3), 639–651.
- Sun, Y., Wang, X., & Tang, X. (2013). Deep convolutional network cascade for facial point detection. In *Proceedings of the 2013 IEEE conference on computer vision and pattern recognition* (pp. 3476–3483).
- Tapia, G., & Elwany, A. (2014). A review on process monitoring and control in metal-based additive manufacturing. *Journal of Manufacturing Science and Engineering*, 136(6), 060801.
- Tsai, K.-M., & Luo, H.-J. (2017). An inverse model for injection molding of optical lens using artificial neural network coupled with genetic algorithm. *Journal of Intelligent Manufacturing*, 28(2), 473–487.
- Xiong, J., Zhang, G., Hu, J., & Wu, L. (2014). Bead geometry prediction for robotic GMAW-based rapid manufacturing through a neural network and a second-order regression analysis. *Journal of Intelligent Manufacturing*, 25(1), 157–163.
- YLR-AC 400W Datasheet. (2018). *IPG Photonics*, <http://www.ipgphotonics.com>. Accessed 12 Apr 2018.
- You, D., Gao, X., & Katayama, S. (2015). WPD-PCA-based laser welding process monitoring and defects diagnosis by using FNN and SVM. *IEEE Transactions on Industrial Electronics*, 62(1), 628–636.
- Zeiler, M. D. (2012). ADADELTA: An adaptive learning rate method. *CoRR*, <http://arxiv.org/abs/1212.5701>.
- Zhang, W., Yang, G., Lin, Y., Gupta, M. M., & Ji, C. (2018). On definition of deep learning. In *Paper presented at the World Automation Congress 2018, 3–6 June 2018*. Skamania Lodge, Stevenson, Washington.
- Zhang, Y., Bernard, A., Harik, R., & Karunakaran, K. P. (2017). Build orientation optimization for multi-part production in additive manufacturing. *Journal of Intelligent Manufacturing*, 28(6), 1393–1407.
- Zhao, Y., Sun, J., Gupta, M. M., Moody, W., Lavery, W. H., & Zhang, W. (2017). Developing a mapping from affective words to design parameters for affective design of apparel products. *Textile Research Journal*, 87(18), 2224–2232.